Semiconductor Physics, Quantum Electronics & Optoelectronics, 2026. V. 29, No 1. P. 019-027.

Semiconductor physics

Synthesis of $Ge_{1-x}Sn_x$ and $Ge_{1-x-y}Sn_xC_y$ films by magnetron sputtering followed by laser annealing

V.O. Yukhymchuk*, G.G. Tarasov, M.Ya. Valakh, P.M. Lytvyn, O.Yo. Gudymenko, N.V. Mazur, T.M. Sabov, V.S. Yefanov, V.M. Dzhagan

V. Lashkaryov Institute of Semiconductor Physics, NAS of Ukraine, 41, Nauky Ave., 03028 Kyiv, Ukraine
**Corresponding author e-mail: v.yukhymchuk@gmail.com*

Abstract. $Ge_{1-x}Sn_x$ is a critically important material for creating direct-bandgap semiconductors integrated into silicon photonic platforms. However, the low equilibrium solubility of Sn in Ge and high mechanical strain in $Ge_{1-x}Sn_x$ films currently hinder their commercial application. This work aims to develop a cost-effective method for producing structurally stable $Ge_{1-x}Sn_x$ films with relatively high Sn content by incorporating carbon (C), and to assess the efficiency of non-equilibrium laser annealing for their crystallization. Amorphous $Ge_{1-x}Sn_x$ and $Ge_{1-x-y}Sn_xC_y$ films were deposited on Ge-buffered Si substrates by magnetron sputtering of the corresponding targets. The samples were subjected to rapid laser annealing using a scanning CW laser (λ = 455 nm) with varying energy density (fluence) and regular thermal annealing for comparison. The films were characterized using Raman spectroscopy, X-ray diffraction, scanning electron microscopy, atomic force microscopy, and X-ray photoelectron spectroscopy. Laser annealing is found to be significantly more efficient than thermal annealing, enabling the formation of $Ge_{1-x-y}Sn_xC_y$ films with a substitutional Sn content up to 4.2 at.% and crystallites with a size of 30 nm, which is three times larger than those formed by thermal annealing. Furthermore, the co-incorporation of C significantly improved the surface morphology.

Keywords: $Ge_{1-x-y}Sn_x$, $Ge_{1-x-y}Sn_xC_y$, direct bandgap, magnetron sputtering, laser annealing, stress compensation.

https://doi.org/10.15407/spqeo29.01.019
PACS 63.22.+m, 68.37.Ps, 68.65.Hb, 72.10.Di

Manuscript received 24.11.25; revised version received 07.02.26; accepted for publication 18.03.26; published online 25.03.26.

1. Introduction

$Ge_{1-x}Sn_x$ is a promising material for efficient NIR light absorbers and emitters, as well as being well-suited for integration into silicon-based optoelectronics and nano-electronics [1–3]. Both theoretical and experimental studies have shown that at a certain Sn fraction (typically between 6–10 at.%), crystalline $Ge_{1-x}Sn_x$ compounds undergo a transition from an indirect-bandgap semi-conductor (like Ge) to a direct-bandgap semiconductor [4–6]. The variation in the reported critical values of x [4–6] can be attributed to differences in the parameters of the $Ge_{1-x}Sn_x$ films, namely, mechanical stresses [7], donor doping concentrations [8], and the influence of quantum-size effects resulting from the small grain size [9].

An important feature of $Ge_{1-x}Sn_x$ is that increasing the Sn fraction substitutionally incorporated in the Ge lattice not only facilitates the transition to a direct-bandgap structure but also significantly narrows the bandgap energy. This narrowing enables the use of $Ge_{1-x}Sn_x$-based devices within both short-wavelength infrared (1.5–3 μm) and potentially the long-wavelength infrared (8–15 μm) ranges. This capability could replace expensive $A^{III}B^{V}$ semiconductor technology with cost-effective monolithic Si-integrated technology in the production of photonic devices.

$Ge_{1-x}Sn_x$ materials are highly versatile for opto-electronic applications, namely in photodetectors, light-emitting diodes, and lasers. Additionally, the high charge carrier mobility theoretically predicted for $Ge_{1-x}Sn_x$ has spurred the development of field-effect transistors based on these materials. The potential for monolithic integration with Si electronics has also led to studies of their thermoelectric applications [10]. Furthermore, these compounds have demonstrated effectiveness as electrodes for lithium-ion batteries [11].

Despite significant advances in the fabrication and study of $Ge_{1-x}Sn_x$ films with a high Sn content, and even the demonstration of laser emission from these materials [12], no commercial devices based on them have been developed to date. This is primarily because the best physical and technical properties of high-quality $Ge_{1-x}Sn_x$

© V. Lashkaryov Institute of Semiconductor Physics of the NAS of Ukraine, 2026
© Publisher PH "Akademperiodyka" of the NAS of Ukraine, 2026

films are achieved only through non-equilibrium synthesis methods such as molecular beam epitaxy (MBE) and chemical vapor deposition (CVD). While these methods are effective, they are expensive and typically geared toward scientific research rather than mass production. Consequently, the current challenge is to develop more cost-effective and technologically simpler methods for fabricating $Ge_{1-x}Sn_x$ films, such as thermal evaporation [13] or magnetron sputtering [14].

A key obstacle to applying these methods is the fundamental issue the low equilibrium solubility of Sn in Ge, which is only 0.5 at.%. This low solubility arises from a significant difference in the covalent radii of Sn (r_{Sn} = 162 pm) and Ge (r_{Ge} = 137 pm). Sn atoms can be incorporated into the Ge lattice only when their concentration does not exceed 0.5 at.%. Beyond this limit, the large lattice mismatch (a_{Sn} is 1.15 times larger than a_{Ge}) introduces high local stresses. This causes Sn atom precipitation, the formation of Sn clusters, and their partial diffusion to the film surface and the film-substrate interface. To overcome this, it is essential to either reduce the lattice mismatch or create conditions in which Sn atoms remain incorporated in the Ge lattice, thereby forming a to compensate for the local stresses that arise metastable solid solution ($Ge_{1-x}Sn_x$). To form $Ge_{1-x}Sn_x$ films on Si substrates with a high Sn content (≥ 6 at. %), it is necessary to compensate for the local stresses that arise in the Ge lattice.

This can be achieved by incorporating atoms with significantly smaller covalent radii than Sn, such as carbon (r_C = 91 pm) or boron (r_B = 82 pm), to create the solid solution $Ge_{1-x-y}Sn_xC_y$ (or $Ge_{1-x-y}Sn_xB_y$). While boron atoms are more effective at stress compensation due to their smaller covalent radius, they also act as acceptor dopants. Thus, their incorporation requires careful consideration of the overall impact on the electronic structure of $Ge_{1-x-y}Sn_xB_y$ and its renormalization, as this can significantly alter film properties. Another approach to obtaining crystalline $Ge_{1-x}Sn_x$ films with high Sn content is forming amorphous $Ge_{1-x}Sn_x$ films, followed by rapid laser annealing. This non-equilibrium annealing process ensures crystallization without significant segregation of Sn atoms.

This work aims to study the crystallization processes of amorphous $Ge_{1-x}Sn_x$ and $Ge_{1-x-y}Sn_xC_y$ films by varying the parameters of laser annealing and to investigate the properties of the resulting films.

2. Experimental technique

p-type Si (100) wafers were used as substrates. A 100 nm thick Ge buffer layer was deposited by magnetron sputtering of the corresponding target on these substrates. Then, the Ge buffer was covered with a 100 nm thick $Ge_{1-x}Sn_x$ layer (the sample structure is schematically shown in Fig. 1a). To obtain optimal characteristics during $Ge_{1-x}Sn_x$ film deposition, the discharge current was varied from 100 to 150 mA, and the temperature of the Si substrate from room temperature to 200 °C.

To dope the $Ge_{1-x}Sn_x$ films with carbon, a thin (~2 nm) carbon layer was incorporated within the film thickness. This was achieved by depositing a 100 nm Ge buffer layer on the Si substrate, followed by a 50 nm $Ge_{1-x}Sn_x$ layer, then the 2 nm carbon layer, which was finally covered with another 50 nm layer of $Ge_{1-x}Sn_x$ (the sample structure is schematically shown in Fig. 1b).

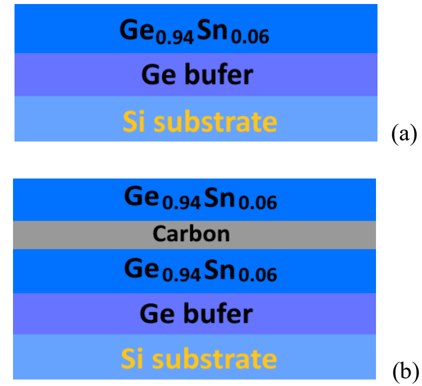

Fig. 1. Schematic representation of the studied $Ge_{1-x}Sn_x$ structures on pre-formed buffer Ge layers on Si substrates: (a) without doping and (b) with carbon doping.

All formed structures were cut into several pieces. Some of them were thermally annealed for 15 min in a nitrogen atmosphere at temperatures from 300 to 600 °C, and the rest were annealed using a CW scanning laser (λ = 455 nm) also in a nitrogen atmosphere. The fluence was varied within 16.0…160.0 J/cm^2. The laser spot was 20 µm wide and 100 µm long, and the scanning speed was equal to 5 mm/s.

The resulting films were characterized using the X-ray diffractometry, Raman spectroscopy, atomic force microscopy (AFM), and scanning electron microscopy (SEM). Raman spectra were recorded using an MDR-23 spectrometer equipped with a TE-cooled CCD detector iDus 401A Andor. The signal was excited by a 532 nm solid-state laser, with a power density on the sample surface not exceeding 10^3 W/cm^2, which excluded thermal modification of the samples. X-ray diffraction (XRD) analysis was performed using a Philips X'Pert PRO-MRD setup with Cu K_α line (λ = 0.15406 nm) in a symmetric (2Θ – ω) mode with a scan step of 0.025 degrees. Surface morphology was studied using a scanning electron microscope Tescan Mira 3 MLU, and a Digital Instruments Nanoscope IIIa AFM system (working in tapping mode, nominal tip radius 10 nm). XPS analyses were carried out using a PHI 5500LS spectrometer with a monochromatic Al K_α (1486.7 eV) source. Calibration yielded a binding energy (BE) of 84 eV for the Au $4f_{7/2}$ line and 932.6 eV for the Cu $2p_{3/2}$ line. Survey scan analysis was carried out with a pass energy of 93.9 eV and a 0.2 eV step. High-resolution spectra were obtained using a pass energy of 11.75 eV and a 0.1 eV step. Before analysis, the samples were pre-etched for 1 min with an Ar^+ ion beam (5 keV, 3×3 mm raster 5 µA).

3. Results and discussion

3.1. Theoretical modelling of the band structure

One of the most critical parameters of $Ge_{1-x}Sn_x$ materials is the bandgap energy, which depends on the Sn atomic content incorporated into the Ge crystal lattice. Numerous studies have calculated the bandgap, both from first principles and using empirical data [15, 16]. In our study, we also carried out theoretical modelling of the band structure of unstrained $Ge_{1-x}Sn_x$ films.

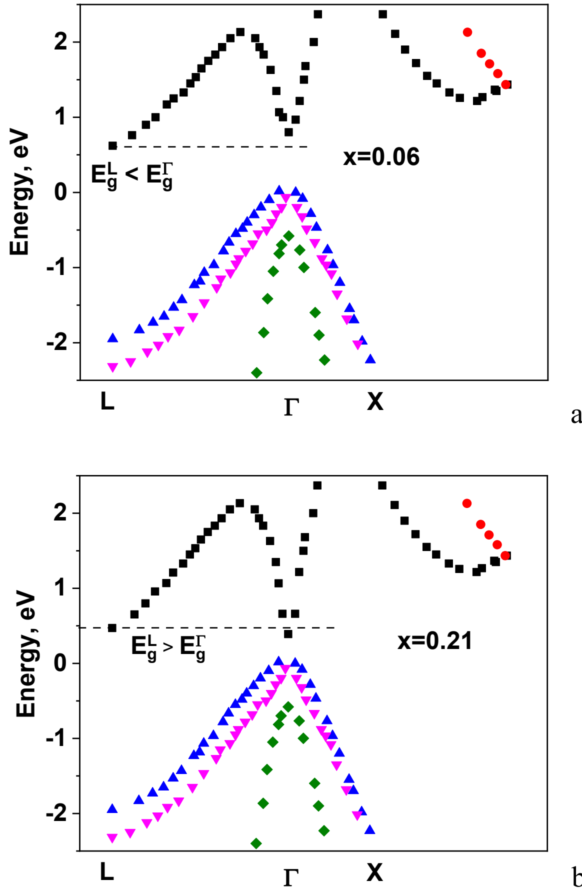

Fig. 2. Calculated electronic structures of $Ge_{1-x}Sn_x$ with different tin contents: (a) x = 0.06 at. % (indirect bandgap); (b) x = 0.21 at. % (direct bandgap).

The band structure of $Ge_{1-x}Sn_x$ was calculated for various Sn fractions (x) using the empirical pseudo-potential method [17, 18]. We employed an 8-band k·p Hamiltonian, in contrast to the traditionally used 6-band k·p Hamiltonian. The 8-band model accounts for the coupling between the conduction and valence bands, which is crucial for accurate calculations.

This Hamiltonian, as proposed in [17], was used in conjunction with the adjustable parameters from [18] to calculate the electronic band structure of $Ge_{1-x}Sn_x$ along symmetry lines in the Brillouin zone for various Sn concentrations, by diagonalizing the Hamiltonian.

Fig. 2a displays the calculated band structure of $Ge_{1-x}Sn_x$ with x = 0.06, corresponding to an indirect bandgap, while Fig. 2b illustrates, as an example, the electronic structure for x = 0.21, which already corresponds to a direct bandgap. Fig. 2 clearly demonstrates that increasing the tin content in the Ge lattice results in a dramatic change in the electronic structure of $Ge_{1-x}Sn_x$, specifically a transition from an indirect bandgap to a direct bandgap. The selected Sn fraction (x = 0.21) corresponds to one of the highest values reported in the literature [19]. With this tin content, the $Ge_{1-x}Sn_x$ material is undoubtedly a direct-bandgap semiconductor. To more precisely determine the Sn fraction in the Ge lattice at which this transition occurs, we plotted the dependence of the bandgap energy

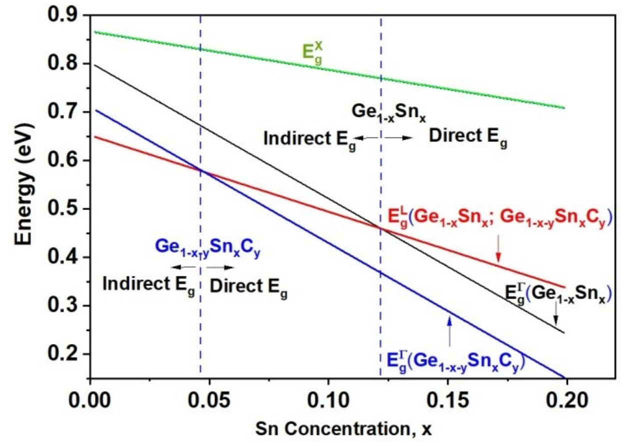

Fig. 3. Sn-concentration dependence of the Γ, L, and X valley energies in $Ge_{1-x}Sn_x$ and $Ge_{1-x-y}S_xC_y$ (0.8 at.% C) structures.

on the Sn content (Fig. 3), along with the impact of co-doping with carbon atoms. The results show that introducing both tin and carbon atoms into the Ge lattice significantly reduces the amount of tin needed for the transition from an indirect-bandgap to a direct-bandgap electronic structure [20].

Calculations using this method revealed that for $Ge_{1-x}Sn_x$, the transition from an indirect to a direct bandgap occurs at x = 0.12. For $Ge_{1-x-y}Sn_xC_y$, the transition happens at x = 0.045 and y = 0.008. Thus, incorporating carbon atoms into the Ge crystal lattice not only reduces the local stresses caused by Sn atom incorporation but also significantly alters the electronic structure, lowering the Sn fraction required for the transition to a direct-bandgap semiconductor.

As highlighted in the introduction of this study, it is crucial to form and experimentally investigate the properties of $Ge_{1-x}Sn_x$ films co-doped with carbon. Notably, due to their much smaller covalent radius compared to Ge, carbon atoms are incorporated into the Ge lattice less readily than Sn atoms, with an equilibrium concentration of only ~10^8 cm^{-3} [21]. Therefore, selecting the correct Sn/C ratio is critical, as exceeding the critical concentration will lead to carbon precipitation, forming clusters, and triggering the precipitation of Sn atoms [22].

3.2. Experimental studies

Fig. 4 shows the Raman spectra of $Ge_{1-x-y}Sn_xC_y$ films formed on a Ge buffer by magnetron sputtering, thermally annealed at temperatures from 300 to 600 °C. The initial film and the film after thermal annealing at 300 °C are amorphous. Annealing the initial film at 400 °C leads to its crystallization, evidenced by the appearance of an intense band corresponding to the Ge–Ge vibrational mode at 297.7 cm^{-1} and a less intense band at 266 cm^{-1}, corresponding to the Ge–Sn vibrational mode. Annealing at 500 °C also results in crystallization, but the Ge–Ge band occurs at 298.2 cm^{-1}. Since the frequency position of this band depends on the tin content in the $Ge_{1-x-y}Sn_xC_y$ film, its shift to the high-frequency side is associated with the partial segregation

of tin from the Ge lattice. A further increase in annealing temperature to 600 °C shifts the Ge–Ge band to 299 cm^{-1}, which is attributed to significant segregation of both tin and carbon atoms. The latter is evidenced by the appearance of bands at 1545 and 1710 cm^{-1} (see the inset to Fig. 4), which are attributed to vibrations of amorphous carbon and C = O bonds, respectively.

The content of Sn atoms incorporated into the Ge lattice can be estimated from the frequency position of the Ge–Ge band using the following formula (1), provided in [23]:

$$\omega^{\text{Ge-Ge}}_{\text{GeSn(x)}} = \omega^{\text{Ge-Ge}}_{\text{Ge bulk}} - \alpha x, \qquad (1)$$

where $\omega^{\text{Ge-Ge}}_{\text{GeSn}(x)}$ is the Ge–Ge Raman peak frequency for the alloy, $\omega^{\text{Ge-Ge}}_{\text{Ge bulk}}$ is the peak frequency for pure Ge, α is a constant, and x is the Sn fraction. This formula does not account for internal stresses that may be present in the film. According to this formula, Sn fraction in the film annealed at 400 °C is 4.0 at.%, and after annealing at 500 °C, the content decreases to 3.2 at.%.

If the mechanical stresses present in the film are considered, the following formula should be used [24]:

$$\omega^{\text{Ge-Ge}}_{\text{GeSn(x)}} = \omega^{\text{Ge-Ge}}_{\text{Ge bulk}} - \alpha x - \beta \varepsilon, \qquad (2)$$

where $\alpha = 82 \pm 4\ cm^{-1}$, $\beta = -563 \pm 5\ cm^{-1}$, and ε is the elastic strain. This formula is well-suited for pseudomorphic films. In our case, the films are polycrystalline and relax during the annealing process. However, as shown in [25], stresses may still be present in polycrystalline Ge films due to the different coefficients of thermal expansion of crystallites at the crystallization temperature and room temperature. The magnitude of these stresses can be estimated according to the formula [25]:

$$\varepsilon = \frac{\Delta\alpha \cdot \Delta T}{1 - \nu}, \qquad (3)$$

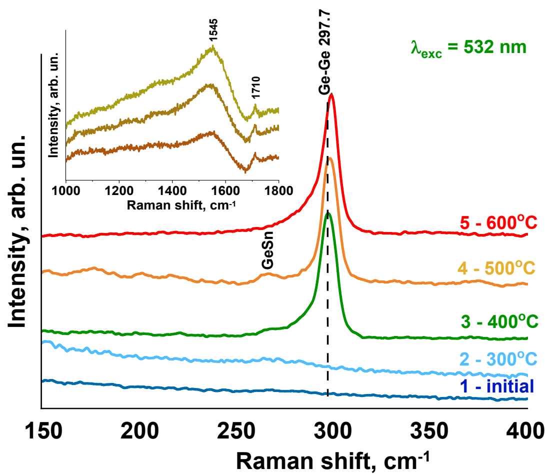

Fig. 4. Raman spectra of $Ge_{1-x-y}Sn_xC_y$ films formed by magnetron sputtering of a $Ge_{1-x}Sn_x$ target and C onto a Ge buffer. Films were thermally annealed at temperatures from 300 to 600 °C. The inset shows the spectra at different points on the surface of the sample annealed at 600 °C within the range of C–C and C–O vibrations.

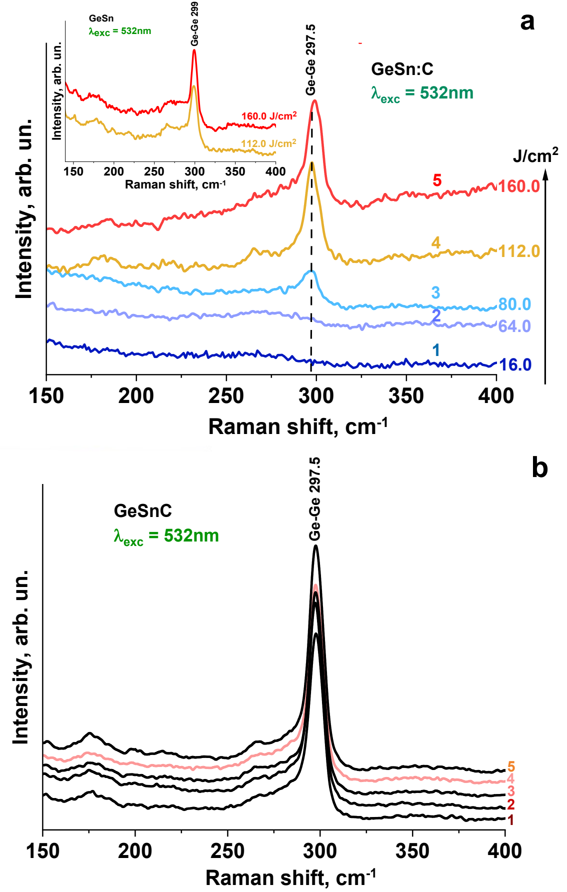

Fig. 5. (a) Raman spectra of $Ge_{1-x-y}Sn_xC_y$ films annealed by a scanning CW laser with fluence density from 16 to 160 J/cm^2. The inset shows the spectra of the $Ge_{1-x}Sn_x$ films annealed with fluences of 112 and 160 J/cm^2. (b) Raman spectra of $Ge_{1-x-y}Sn_xC_y$ films annealed by a scanning CW laser at 112 J/cm^2 at different points on the film.

where α is the coefficient of thermal expansion, $\Delta\alpha = \alpha_{\text{film}} - \alpha_{\text{substrate}}$ ($\Delta\alpha \approx 1.0 \cdot 10^{-6}\ °C^{-1}$ in our case), ΔT is the difference between the annealing temperature (400 °C) and room temperature (20 °C), ν = 0.27 is the Poisson ratio of the Ge film [26]. According to (2) and (3), the substitutional Sn fraction is 3.0 and 2.1 at.% in $Ge_{1-x-y}Sn_xC_y$ films annealed at 400 °C and 500 °C, respectively. Thus, according to (1) and (2), for films annealed at 400 °C, the content of Sn in the Ge lattice is within the range 3.0…4.0 at.%.

Earlier, we have shown [13] that annealing of GeSn films using scanning laser is more effective compared to thermal annealing. Therefore, we performed annealing of $Ge_{1-x-y}Sn_xC_y$ films using a continuous scanning laser with λ = 455 nm. During annealing, the laser fluence was from 16 to 160 J/cm^2.

As seen from Fig. 5a, if $Ge_{1-x-y}Sn_xC_y$ films are annealed with a laser fluence up to 64 J/cm^2, they remain completely amorphous (only a broad band at 271 cm^{-1} appears in the spectrum). At a fluence of 80 J/cm^2, an additional band caused by the crystalline phase at 297 cm^{-1} appears in the spectrum. The optimal laser fluence has been established to be 112 J/cm^2. A further increase in the laser fluence leads to a gradual shift of the

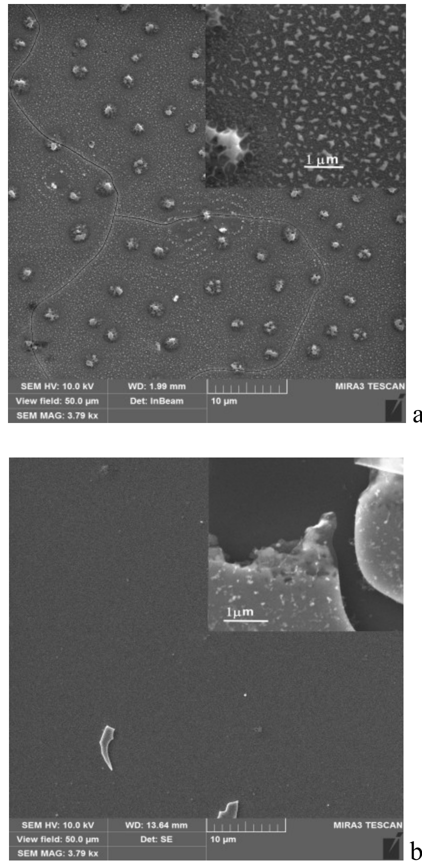

Fig. 6. SEM images of the surface of (a) $Ge_{1-x}Sn_x$ and (b) $Ge_{1-x-y}Sn_xC_y$ films annealed by a CW scanning laser with a fluence of 112 J/cm^2. The insets show a magnified image of these surfaces.

Ge–Ge bands to high frequencies (Fig. 5a, curve *5*), indicating partial segregation of tin from the Ge crystal lattice.

Registration of Raman spectra at different points on the surface of the annealed film showed that the film is homogeneous within the error range (Fig. 5b).

Estimation of the elemental composition of the formed film according to (1) and (2) yielded that the content of incorporated tin atoms in the Ge lattice is between 3.2 and 4.4 at.%. This value is close to the theoretically calculated value for $Ge_{1-x-y}Sn_xC_y$, at which the transition to a direct-bandgap semiconductor occurs.

The Raman spectra of $Ge_{1-x}Sn_x$ films (see inset in Fig. 5a) annealed under the same conditions as $Ge_{1-x-y}Sn_xC_y$ are similar to the spectra of the ternary alloy, although the Ge–Ge band frequencies are slightly higher. This indicates that, in this case, a lower percentage (~3 at.%) of tin atoms is incorporated into the Ge lattice.

Fig. 6 shows SEM images of the surface of $Ge_{1-x}Sn_x$ (a) and $Ge_{1-x-y}Sn_xC_y$ (b) films annealed using a scanning laser with a fluence of 112 J/cm^2. Fig. 6a shows that the surface of the $Ge_{1-x}Sn_x$ film exhibits uniformly distributed "large" islands with sizes of 1-2 µm and a density of $2.5 \cdot 10^7$ cm^{-2}, around which the smaller islands are visible. It is worth noting that the "small" islands are arranged in concentric circles around the "large" islands. The height of the latter, estimated by AFM studies (image not shown), is small, only 4-6 nm. These are most likely areas with significant Sn and C segregation.

The formation of this morphology can be explained by the following mechanism: The "large" islands create significant local inhomogeneity on the film surface, absorbing laser radiation more efficiently and, accordingly, heating up more strongly. This creates a strong radial temperature gradient around them. In most liquids (including semiconductor melts), surface tension decreases with increasing temperature. Consequently, the $Ge_{1-x-y}Sn_xC_y$ film melt begins to move from areas with lower surface tension (hotter areas) to areas with higher surface tension (colder areas). Thus, convective flows (a manifestation of the Marangoni effect [27]) arise around large islands, circulating along the radii and capturing and transporting dissolved Sn or C atoms. The dynamics of the convection flow in a thin liquid film can lead to hydrodynamic instabilities resulting in the formation of stationary or oscillating structures, the so-called convection cells (rolls/cells). Upon cooling and rapid recrystallization, these cells lead to the periodic accumulation of material (Sn-rich phases) in the form of rings of "small" islands around the initial "large" island. Thus, the "large" island acts as a center that sets a radial thermal gradient, which triggers a thermocapillary flow, leading to formation of an ordered ring structure of smaller islands. It should be noted that cracks are also observed on the surface of the $Ge_{1-x-y}Sn_xC_y$ film, which were formed during the annealing process, as the $Ge_{1-x-y}Sn_xC_y$ film is formed on a strained Ge buffer layer. Raman spectra of the $Ge_{1-x}Sn_x$ film (without carbon) annealed by a laser (inset in Fig. 5a) indicate that the Sn content in the Ge lattice is approximately 1 at.% smaller compared to the $Ge_{1-x-y}Sn_xC_y$.

The morphology of the $Ge_{1-x-y}Sn_xC_y$ film annealed under the same laser conditions is significantly different. Neither "large" islands nor cracks appear on the film surface. At high magnification (inset in Fig. 6b), islands with average sizes of ~100 nm are visible, randomly distributed over the surface. Apparently, the addition of C atoms changes the phase transition mechanism during laser annealing from the growth of a few large islands (due to strong Sn segregation) to the controlled nucleation and growth of many small, homogeneous crystalline islands (~100 nm), which significantly

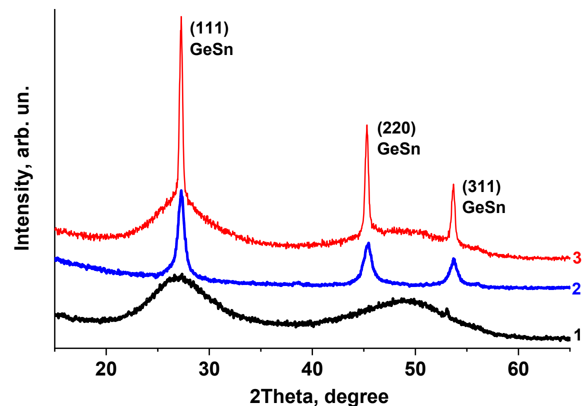

Fig. 7. XRD of $Ge_{1-x-y}Sn_xC_y$ films: (*1*) as grown, (*2*) thermally annealed at 400 °C, (*3*) annealed by scanning laser radiation (λ = 455 nm) at a fluence of 112 J/cm^2.

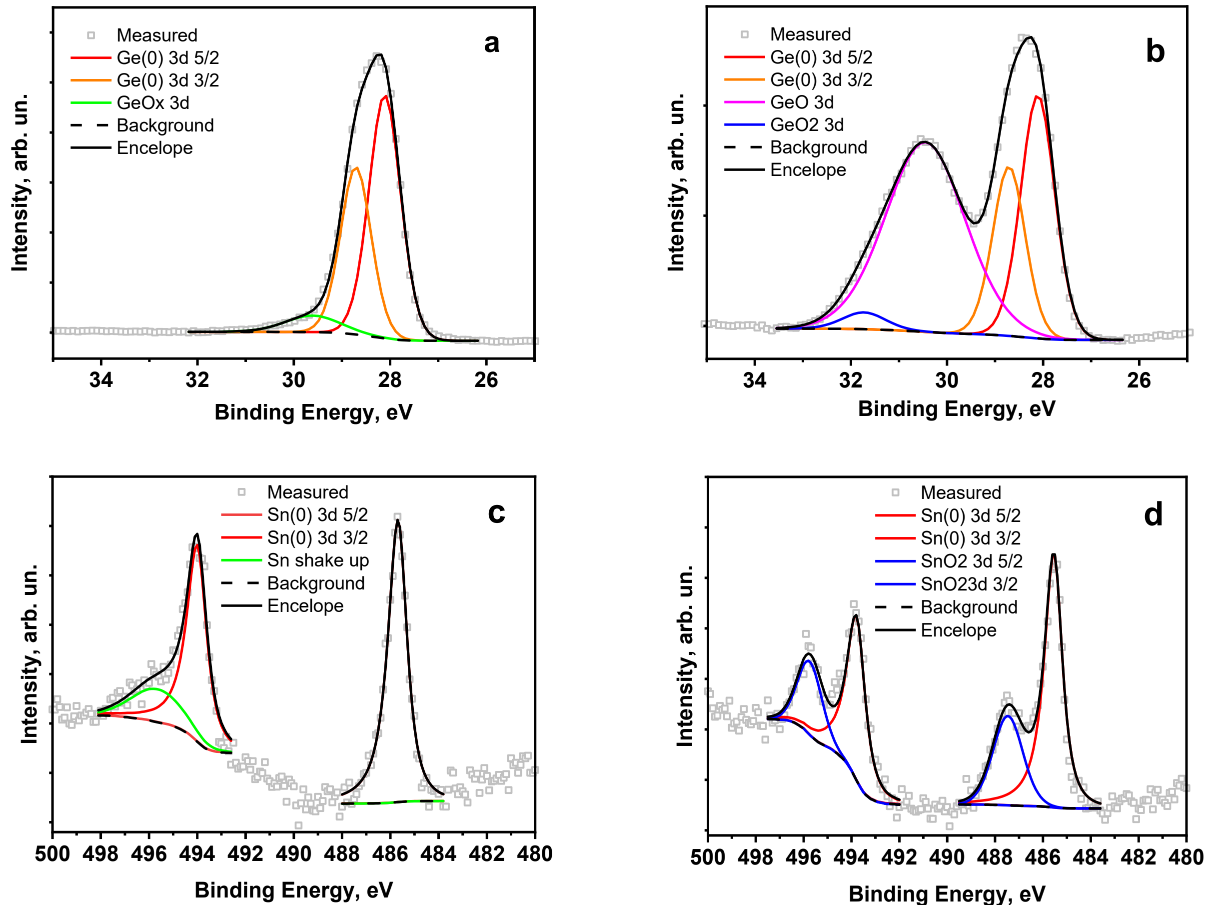

Fig. 8. XPS Ge 3d spectra of as-grown (a) and annealed at 600 °C $Ge_{1-x}Sn_x$ samples (b); XPS Sn 3d spectra of as-grown (c) and annealed at 600 °C $Ge_{1-x}Sn_x$ samples (d).

improves the surface morphology. The reduction of Sn segregation and stress compensation due to C incorporation makes the film more mechanically stable during rapid thermal annealing, preventing the formation of macroscopic cracks.

Fig. 7 shows the diffraction patterns of the initial $Ge_{1-x-y}Sn_xC_y$ film as well as after thermal and laser annealing. The XRD study confirms that the initial film is completely amorphous. Thermal annealing in a nitrogen atmosphere at 400 °C leads to its crystallization. To ensure effective XRD measurement, laser annealing of these films was carried out over a 1 cm^2 area of a 1.7 cm^2 sample with a fluence of 112 J/cm^2. In this case laser annealing also leads to its complete crystallization. The presence of an amorphous component in this diffractogram is due to the presence of the sample edges that were not subjected to laser scanning. This laser annealing has a potentially important application, namely the possibility of performing crystallization locally without heating the entire sample to high temperatures, as during thermal annealing.

Another important advantage of laser annealing is the formation of a more perfect crystalline structure compared to the structure obtained with thermal annealing, which is reflected in significantly smaller full widths at half maximum (FWHM) of the reflections. The average size of coherent scattering regions (crystallites), *D*, was calculated using the Scherrer formula [28]:

$$D = (K \times \lambda)/(b \times \cos\theta), \tag{4}$$

where λ is the X-ray wavelength, β is the FWHM of the reflection (in radians), θ is the Bragg angle, and *K* is the dimensionless particle shape coefficient. The results indicate that the crystallite size is ~10 nm for materials formed by thermal annealing and ~30 nm for those formed by laser annealing.

Fig. 8 shows high-resolution XPS spectra and their decomposition on individual components for the initial and thermally annealed at 600 °C $Ge_{1-x}Sn_x$ film. From the general XPS spectra, it was found that the initial film contains Ge, Sn, and C, and after its annealing, oxygen also appears. The Sn concentration in the initial film is 2.5 at.%, and after annealing, it increases to 4.3 at.%.

The deconvolution of XPS spectra of the initial film (Fig. 8a) showed that the observed peaks correspond to metallic Ge(0) $3d_{5/2}$, Ge(0) $3d_{3/2}$, and GeO_x 3d [29, 30]. Ge is mainly in the metallic state, with a Ge–Ge bond content of 93.45 at.%. Annealing leads to the formation of an oxide film on the surface, as evidenced by the appearance of peaks corresponding to GeO and GeO_2 (Fig. 8b). Oxygen required

for the formation of oxides can originate from the residual furnace atmosphere and impurities in the carrier gas (N_2), as well as from the initial native oxide layer on the film surface. Figs. 8c and 8d show the XPS Sn 3d spectra from films before and after annealing. One can see that Sn is in the metallic phase before annealing, and the SnO_2 phase is formed after annealing. The Sn(0)/SnO_2 phase ratio was 68.6/31.4 at.%.

Thus, studies on $Ge_{1-x}Sn_x$ and $Ge_{1-x-y}Sn_xC_y$ films formed by magnetron sputtering followed by annealing using a scanning continuous laser indicate the possibility of forming $Ge_{1-x}Sn_x$ films with a high tin content (~4 at.%). The effectiveness of laser annealing for providing non-equilibrium processes, namely, the transformation of the amorphous $Ge_{1-x-y}Sn_xC_y$ phase into a crystalline one without significant tin segregation, has been confirmed.

The issue of determining the optimal Sn/C ratio in as-grown amorphous films with increasing the proportion of Sn relative to Ge remains relevant. Measuring the photoluminescence spectra of these films will allow us to definitively confirm the transformation from an indirect-bandgap structure to a direct-bandgap one.

4. Conclusions

This work theoretically analyzed the change in the bandgap energy upon the incorporation of both tin atoms and simultaneously tin and carbon atoms into the Ge crystal lattice. The results show that introducing a small amount of carbon into the Ge lattice significantly reduces the amount of tin needed for the transition from an indirect-bandgap to a direct-bandgap structure.

The possibility of forming polycrystalline $Ge_{1-x}Sn_x$ and $Ge_{1-x-y}Sn_xC_y$ films by magnetron sputtering on a Ge buffer formed on a Si substrate, followed by laser annealing, has been experimentally demonstrated. Raman spectroscopy and XRD results showed that annealing of amorphous $Ge_{1-x}Sn_x$ and $Ge_{1-x-y}Sn_xC_y$ films using scanning continuous laser radiation is significantly more effective than thermal annealing. This advantage is evidenced by the following. Laser annealed $Ge_{1-x-y}Sn_xC_y$ films are more crystallographically perfect compared to films that were thermally annealed, evidenced by the smaller FWHMs of XRD reflections and the larger size of nanocrystallites (30 nm *versus* 10 nm). Laser annealing allows obtaining $Ge_{1-x-y}Sn_xC_y$ films with a slightly larger (~0.4 at.%) content of tin atoms in the Ge lattice.

It was demonstrated that the simultaneous incorporation of tin and carbon atoms significantly changes the morphology of the film surface during laser annealing. It was shown that "large" (~1–2 µm in diameter) islands caused by the segregation of Sn and C atoms and macroscopic cracks are not formed in the $Ge_{1-x-y}Sn_xC_y$ films. Using XPS spectroscopy, it was shown that thermal annealing at 600 °C in a nitrogen atmosphere leads to the formation of germanium and tin oxides, which may be due to the presence of oxygen in the residual furnace atmosphere and impurities in the carrier gas (N_2), as well as from the initial native oxide layer on the film surface.

Thus, the magnetron sputtering method in combination with scanning laser annealing is promising for the creation of polycrystalline $Ge_{1-x-y}Sn_xC_y$ films. Carbon doping effectively compensates for lattice strain, stabilizes the metastable solid solution, and provides a pathway for achieving direct-bandgap GeSn materials at lower tin concentrations.

Acknowledgments

The work by V.Yu., G.T., O.G., N.M., T.S., and V.Ye. was supported by the National Research Foundation of Ukraine (Project No. 2023.03/0186 "Deformation engineering of the electronic structure of GeSn thin films for new generation IR. Optoelectronics"). The authors are also grateful to Dr. M.A. Skoryk for SEM measurements of the samples.

References

1. Margetis J., Al-Kabi S., Du W. *et al*. Si-based GeSn lasers with wavelength coverage of 2–3 µm and operating temperatures up to 180 K. *ACS Photonics*. 2018. **5**. P. 827. https://doi.org/10.1021/acsphotonics.7b00938.
2. Chou M.-H., Bansal R., Jheng Yu. *et al*. High-detectivity GeSn mid-infrared photodetectors for sensitive infrared spectroscopy. *Adv. Photonics Res*. 2025. **6**. P. 2400155. https://doi.org/10.1002/adpr.202400155.
3. Nawwar M.A., Abo Ghazala M.S., Sharaf El-Deen L.M., Kashyout A.E.B. Impact of strain engineering and Sn content on GeSn heterostructured nanomaterials for nanoelectronics and photonic devices. *RSC Adv*. 2022. **12**, No 38. P. 24518. https://doi.org/10.1039/d2ra04181b.
4. Dutt B., Lin H., Sukhdeo D.S. *et al*. Theoretical analysis of GeSn alloys as a gain medium for a Si-compatible laser. *IEEE J. Sel. Top. Quantum Electron*. 2013. **19**, No 5. P. 1502706. https://doi.org/10.1109/JSTQE.2013.2241397.
5. Moontragoon P. *et al*. Band structure calculations of Si–Ge–Sn alloys: achieving direct band gap materials. *Semicond. Sci. Technol*. 2007. **22**. P. 742. https://doi.org/10.1088/0268-1242/22/7/012.
6. Kasper E., Kittler M., Oehme M., Arguirov T. Germanium tin: silicon photonics toward the mid-infrared. *Photon. Res*. 2013. **1**, No 2. P. 69. https://doi.org/10.1364/PRJ.1.000069.
7. Moontragoon P., Soref R.A., Ikonic Z. The direct and indirect bandgaps of unstrained $Si_xGe_{1-x-y}Sn_y$ and their photonic device applications. *J. Appl. Phys*. 2012. **112**. P. 073106. https://doi.org/10.1063/1.4757414.
8. Prucnal S., Berencén Yo., Wan M. *et al*. Strain and band-gap engineering in Ge-Sn alloys *via* P doping. *Phys. Rev. Appl*. 2018. **10**. P. 064055. https://doi.org/10.1103/PhysRevApplied.10.064055.
9. Stange D., von den Driesch N., Rainko D. *et al*. Quantum confinement effects in GeSn/SiGeSn heterostructure lasers. *2017 IEEE International Electron Devices Meeting (IEDM)*, San Francisco, CA, USA, 2017. P. 24.2.1–24.2.4. https://doi.org/10.1109/IEDM.2017.8268451.
10. Spirito D., von den Driesch N., Manganelli C.L. *et al*. Thermoelectric efficiency of epitaxial GeSn alloys for integrated Si-based applications: Assessing the lattice thermal conductivity by Raman thermometry. *ACS Appl. Energy Mater*. 2021. **4**, No 7. P. 7385. https://doi.org/10.1021/acsaem.1c01576.

11. Doherty J., McNulty D., Biswas S. *et al*. Germanium tin alloy nanowires as anode materials for high performance Li-ion batteries. *Nanotechnology.* 2020. **31**. P. 165402. https://doi.org/10.1088/1361-6528/ab6678.
12. Chretien J., Thai Q.M., Frauenrath M. *et al*. Room temperature optically pumped GeSn microdisk lasers. *Appl. Phys. Lett*. 2022. **120**. P. 051107. https://doi.org/10.1063/5.0074478.
13. Yukhymchuk V., Lytvyn P., Korchovyi A. *et al*. Laser-induced crystallisation of amorphous GeSn and GeSn:C films. *Mater. Res. Express*. 2025. **12**. P. 115004. https://doi.org/10.1088/2053-1591/ae1d3d.
14. Huang H., Zhao D., Qi C. *et al*. Effect of growth temperature on crystallization of $Ge_{1-x}Sn_x$ films by magnetron sputtering. *Crystals.* 2022. **12**. P. 1810. https://doi.org/10.3390/cryst12121810.
15. Huang W., Cheng B., Xue C., Liu Z. Comparative studies of band structures for biaxial (100)-, (110)-, and (111)-strained GeSn: A first-principles calculation with GGA+U approach. *J. Appl. Phys.* 2015. **118**. P. 165704. https://doi.org/10.1063/1.4933394.
16. Wang X., Chen C., Feng S. *et al*. A hybrid functional first-principles study on the band structure of non-strained $Ge_{1-x}Sn_x$ alloys. *Chin. Phys. B*. 2017. **26**, No 12. P. 127402. https://10.1088/1674-1056/26/12/127402.
17. Low K.L., Yang Yu., Han G. *et al*. Electronic band structure and effective mass parameters of $Ge_{1-x}Sn_x$ alloys. *J. Appl. Phys.* 2012. **112**. P. 103715. https://doi.org/doi.org/10.1063/1.4767381.
18. Ridene S., Boujdaria K., Bouchriha H., Fishman G. Infrared absorption in $Si/Si_{1-x}Ge_x/Si$ quantum wells. *Phys. Rev. B*. 2001. **64**. P. 085329. https://doi.org/10.1103/PhysRevB.64.085329.
19. Rosson N., Acharya S., Fischer A.M. *et al*. Development of GeSn epitaxial films with strong direct bandgap luminescence in the mid-wave infrared region using a commercial chemical vapor deposition reactor. *J. Vac. Sci. Technol. B*. 2024. **42**. P. 052210. https://doi.org/10.1116/6.0003798.
20. Dey T., Reza Md.S., Arbogast A. *et al*. Molecular beam epitaxy of highly crystalline GeSnC using CBr_4 at low temperatures. *Appl. Phys. Lett*. 2022. **121**, Issue 12. P. 122104. https://doi.org/10.1063/5.0102093.
21. Wei P. *et al*. Structure and optical properties of germanium implanted with carbon ions**.** *Nucl. Instrum. Methods Phys. Res. B***.** 2003. **206**. P. 233. https://doi.org/10.1016/S.0168-583X(03)00738-9.
22. Yukhymchuk V.O., Gudymenko O.Yo., Sabov T.M. *et al*. Formation and properties of GeSn:C films on silicon substrates. *SPQEO*. 2024. **27**. P. 412. https://doi.org/10.15407/spqeo27.04.412.
23. D'Costa V.R., Tolle J., Roucka R. *et al*. Raman scattering in $Ge_{1-y}Sn_y$ alloys. *Solid State Commun.* 2007. **144**. P. 240–244. https://doi.org/10.1016/j.ssc.2007.08.020.
24. Lin H., Chen R., Huo Yi. *et al*. Raman study of strained $Ge_{1-x}Sn_x$ alloys. *Appl. Phys. Lett*. 2011. **98**. P. 261917. https://doi.org/10.1063/1.3606384.
25. Imajo T., Suemasu T., Toko K. Strain effects on polycrystalline germanium thin films. *Sci. Rept.* 2021. **11**. P. 8333. https://doi.org/10.1038/s41598-021-87616-x.
26. Zhang X., Xu F., Mu Z. *et al*. In-situ measurement of Poisson's ratio for germanium nano-bridge in TEM. *2016 Symposium on Design, Test, Integration and Packaging of MEMS/MOEMS (DTIP).* Budapest, Hungary, 30 May – 2 June 2016. https://10.1109/DTIP.2016.7514834.
27. Roché M., Li Z., Griffiths I.M. *et al*. Marangoni flow of soluble amphiphiles. *Phys. Rev. Lett*. 2014. **112**. P. 208302. https://doi.org//10.1103/PhysRevLett.112.208302.
28. Langford J.I., Wilson A.J.C. Scherrer after sixty years: a survey and some new results in the determination of crystallite size. *J. Appl. Crystallogr*. 1978. **11**, No 2. P. 102. http://doi.org/10.1107/s0021889878012844.
29. Germanium X-ray photoelectron spectra, germanium electron configuration, and other elemental information. https://www.thermofisher.com/ua/en/home/materials-science/learning-center/periodic-table/metalloid/germanium.html.
30. Basic XPS Information Section. https://xpsdatabase.net/germanium-ge-z32-germanium-compounds.

Authors and CV

Volodymyr O. Yukhymchuk, Prof., Dr. Sci., Head of Optics and Spectroscopy Department at the V. Lashkaryov Institute of Semiconductor Physics. Authored over 300 publications. Expertise: optical and vibrational spectroscopy, Raman scattering, SERS, plasmonics, luminescence, semiconductors, nanostructures.
https://orcid.org/0000-0002-5218-9154

Georgiy G. Tarasov. Professor at the V. Lashkaryov Institute of Semiconductor Physics. Current research interest is the physics of low-dimensional structures (quantum wells, dots, and wires), spin-doped compounds, and heterostructures.
E-mail: georgiy_tarasov@yahoo.com,
https://orcid.org/0000-0001-8792-1555

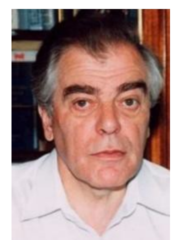

Mykhailo Ya. Valakh, Prof., Dr. Sci., Corresponding Member of the NAS of Ukraine. He is the author of more than 400 scientific publications, 7 patents, and 5 textbooks. The area of his scientific interests includes physics of semiconductors and dielectrics, optics and spectroscopy of solid state, materials science for electronics, physics of nanostructures, and optical diagnostics of materials. E-mail: mvalakh@gmail.com,
https://orcid.org/0000-0003-3849-3499

Petro M. Lytvyn, PhD, Head of Department at the V. Lashkaryov Institute of Semiconductor Physics. His research focuses on solid-state physics, functional materials, and nanophysics of semiconductors and related materials. Authored over 350 peer-reviewed publications, 9 monographs and 10 patents. E-mail:plyt2007@gmail.com, https://orcid.org/0000-0002-0131-9860

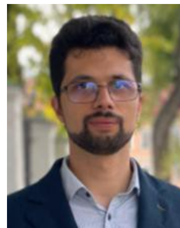

Tomash M. Sabov, PhD, Researcher at the Department of Ion-Beam Engineering, V. Lashkaryov Institute of Semiconductor Physics. Author of more than 20 publications. Field of research: activity is the physics of thin films, chromogenic materials and SIMS analysis.
E-mail: tsabov92@gmail.com,
https://orcid.org/0000-0003-2636-2379

Olexandr Yo. Gudymenko, PhD, Senior Researcher at the Department of Ion-Beam Engineering, V. Lashkaryov Institute of Semiconductor Physics. Author of more than 60 publications. Field of research: solid-state physics, dynamical theory of diffraction of radiation, X-ray optics, X-ray diffraction analysis of semiconductor crystals.
E-mail: gudymen@ukr.net,
https://orcid.org/ 0000-0002-5866-8084

Volodymyr S. Yefanov, PhD in Physics and Mathematics, Senior Researcher at the Department of Optics and Spectroscopy, V. Lashkaryov Institute of Semiconductor Physics. Research interests include electronic transport properties and their relationship with structural transformations in semiconductor materials.
E-mail: vyefanov@gmail.com,
https://orcid.org/0000-0001-5408-1086

Nazar M. Mazur, PhD (Applied Physics and Nanomaterials, 2021), Researcher at the V. Lashkaryov Institute of Semiconductor Physics. Authored over 30 articles and 10 patents. The area of his scientific interests includes semiconductors, Raman spectroscopy, and nanomaterials.
E-mail:nazarmazur1994@gmail.com,
https://orcid.org/0000-0001-5331-1628

Volodymyr M. Dzhagan, Dr.Sci., Prof., Acting Deputy Director of the V. Lashkaryov Institute of Semiconductor Physics. Authored over 200 publications. Expertise: optical and vibrational properties of semiconductors, nanostructures, and composite materials.
E-mail: dzhagan@isp.kiev.ua,
https://orcid.org/0000-0002-7839-9862

Authors' contributions

Yukhymchuk V.O: conceptualization, supervision.
Tarasov G.G.: theoretical calculations.
Valakh M.Ya.: conceptualization.
Lytvyn P.M.: AFM investigation; laser annealing.
Gudymenko O.Yo.: XRD investigation, data analysis.
Mazur N.V.: Raman measurements, data analysis.
Sabov T.M.: XPS study of films.
Yefanov V.S.: writing – review and editing.
Dzhagan V.M.: conceptualization.

Синтез плівок $Ge_{1-x-y}Sn_x$ та $Ge_{1-x-y}Sn_xC_y$ методом магнетронного розпилення з подальшим лазерним відпалом

В.О. Юхимчук, Г.Г. Тарасов, М.Я. Валах, П.М. Литвин, О.Й. Гудименко, Н.В. Мазур, Т.М. Сабов, В.С. Єфанов, В.М. Джаган

Анотація. $Ge_{1-x}Sn_x$ є критично важливим матеріалом для створення прямозонних напівпровідників, інтегрованих у кремнієві фотонні платформи. Однак низька рівноважна розчинність Sn у Ge та високі механічні напруження в плівках $Ge_{1-x}Sn_x$ наразі перешкоджають їх комерційному застосуванню. Метою цієї роботи є розробка економічно ефективного методу отримання структурно стабільних плівок $Ge_{1-x}Sn_x$ з відносно високим вмістом олова шляхом додавання вуглецю (C) та оцінка ефективності нерівноважного лазерного відпалу для їх кристалізації. Аморфні плівки $Ge_{1-x}Sn_x$ та $Ge_{1-x-y}Sn_xC_y$ були нанесені на Ge-буферизовані Si підкладки методом магнетронного розпилення відповідних мішеней. Зразки піддавали швидкому відпалу за допомогою скануючого CW лазера ($\lambda = 455$ нм) зі змінною густиною енергії, а також звичайному термічному відпалу для порівняння. Плівки досліджено за допомогою раманівської спектроскопії, рентгенівської дифракції, скануючої електронної мікроскопії, атомно-силової мікроскопії та рентгенівської фотоелектронної спектроскопії. Лазерний відпал виявився значно ефективнішим за термічний та дозволив формувати плівки $Ge_{1-x-y}Sn_xC_y$ з вмістом олова в Ge ґратці до 4.2 ат.% та кристалітами розміром 30 нм, що втричі більше, ніж ті, що утворилися при термічному відпалі. Крім того, додавання C значно покращило морфологію поверхні.

Ключові слова: $Ge_{1-x}Sn_x$, $Ge_{1-x-y}Sn_xC_y$, пряма заборонена зона, магнетронне розпилення, лазерний відпал, компенсація напружень.